Selective Harmonic Suppression for Finite-Control-Set Model Predictive Control

Martinus Dorfling*, Toit Mouton*, Tobias Geyer†
* Department of Electrical and Electronic Engineering
University of Stellenbosch, Private Bag X1, Matieland, 7602, Stellenbosch, South Africa
Email: mddorfling@sun.ac.za, dtmouton@sun.ac.za
† ABB Corporate Research
Segelhofstrasse 1K, 5405 Baden-Dättwil, Switzerland, Email: t.geyer@ieee.org

Keywords

≪Predictive Control≫, ≪Harmonics≫, ≪Converter control≫, ≪Three-phase system≫

Abstract

For finite-control-set model predictive control with long horizons, a method is proposed that allows targeted harmonics in the current spectrum to be suppressed. The method involves adding band-pass filters at target frequencies, which are then included in the state-space representation of the prediction model. The underlying optimization problem can be efficiently solved with sphere decoding, allowing the use of long horizons to improve the system performance. A case study with a grid-connected converter is presented and simulations are provided that demonstrate the efficacy of the proposed method.

Introduction

Finite-control-set (FCS) model predictive control (MPC), a direct MPC method, has gained significant attention in the power electronics community [1, 2] and has even been discussed in textbooks [3, 4]. In direct MPC methods, the controller directly manipulates the switching state of a converter and therefore a modulator is not required.

Usually, FCS-MPC is implemented with a single-step prediction horizon, in other words, the evolution of the state variables is only predicted for one sampling interval into the future. Although a single prediction step has the benefit of being easy to implement and having a low computational burden, long horizons (i.e. predicting the evolution of the state variables at multiple sampling instants into the future) have been proven to posses superior harmonic distortion performance in comparison with short horizons [5]. Moreover, plants with non-minimum phase behaviour require long horizons to guarantee stability [6].

The primary drawback of long horizons for FCS-MPC is that the number of possible converter switching state combinations increases exponentially with the length of the horizon, making the widely-used exhaustive search method intractable. However, it has been shown that the underlying optimization problem can be reformulated as an integer least-square problem (ILS) [2]. This allows the use of a branch-and-bound method known as sphere decoding, resulting in a significant reduction in time required to find the optimal switching sequence for the converter. The sphere decoder has enabled the practical application of long horizons, being recently implemented in practice on an FPGA [7].

Unfortunately, direct MPC introduces a significant problem for certain applications: the harmonic spectrum is non-deterministic. For grid-connected converters, strict harmonic standards are imposed on the amplitudes of current harmonics at the point of common coupling; meeting these standards is challenging for direct MPC due to its the non-deterministic spectrum. For electrical machines, certain harmonics cause torsional vibrations on the shaft and can cause signification damage [8].

Few MPC methods are available that allow control over the spectrum. One of the first methods for FCS-MPC was the addition of a notch filter at a specified frequency (the notch frequency) [9]. That output of the filter is included in the objective function, which penalises all the frequency components outside the passband of the

filter. The controller shifts most of the harmonic energy into the notch frequency. This results in a switching frequency that is more or less equal to the notch frequency.

Another method specifically for FCS-MPC is to calculate off-line selective harmonic elimination pulse-width modulated patterns, and to then penalise the deviation of the converter switching state from those of the pre-calculated pattern [10]. This results in a steady-state spectrum that represents that of the off-line pattern.

In [11], a short-time Fourier transform of the output is used, and constraints are imposed on the spectrum. This method uses a so-called *extended horizon* for the spectrogram constraints due to the filter window, which increases the computational burden.

This paper will introduce a simple harmonic suppression method for long-horizon FCS-MPC. The method will involve placing band-pass filters at target frequencies. The filters are then included in the state-space representation, which is the dynamic model used by the controller. The filter states containing the targeted harmonics are subsequently penalised in the objective function, resulting in the targeted harmonics being suppressed. The FCS-MPC problem formulation, along with a review of the ILS problem reformulation, is presented. Simulation results when suppressing one or two harmonics are presented.

System Description and Harmonic Suppression Strategy

Modelling of grid-connected neutral-point-clamped converter

A three-phase three-level neutral-point-clamped (NPC) converter connected to a grid is shown in Fig. 1. The dc-link with the dc-link voltage V_d is represented by two voltage sources. This idealised setup implies that the neutral point N of the converter is fixed to zero. The resistor R and inductor L represent the resistance and inductance of the grid, respectively. The former includes the series equivalent resistance (ESR) of the filter inductance. The grid is assumed to be balanced with positive sequence.

The NPC converter can synthesise three voltage levels at any particular phase terminal, with the output phase voltage being

$$v_p = \frac{V_d}{2} u_p, \tag{1}$$

where $u_p \in \mathcal{U}$, with $\mathcal{U} = \{-1, 0, 1\}$, is the switch position of a particular phase $p \in \{a, b, c\}$. The three-phase voltage output can be described with

$$\boldsymbol{v}_{abc} = \frac{V_d}{2} \boldsymbol{u}_{abc}, \tag{2}$$

where $\boldsymbol{v}_{abc} = \begin{bmatrix} v_a & v_b & v_c \end{bmatrix}^{\mathrm{T}}$ and $\boldsymbol{u}_{abc} = \begin{bmatrix} u_a & u_b & u_c \end{bmatrix}^{\mathrm{T}}$. The three-phase switch position is restricted to $\boldsymbol{u}_{abc} \in \mathcal{U}$, where $\mathcal{U} = \mathcal{U} \times \mathcal{U} \times \mathcal{U}$.

By selecting the state variables as $\boldsymbol{x}(t) = \boldsymbol{i}_{\alpha\beta}(t) = \begin{bmatrix} i_\alpha(t) & i_\beta(t) \end{bmatrix}^{\mathrm{T}}$, the grid current can be described in the stationary orthogonal αβ-reference frame by using a continuous-time state-space representation of the plant:

$$\frac{d\boldsymbol{x}(t)}{dt} = \boldsymbol{F}\boldsymbol{x}(t) + \boldsymbol{G}\boldsymbol{u}(t) + \boldsymbol{P}\boldsymbol{v}_g(t), \tag{3}$$

where $\boldsymbol{F} = -\frac{R}{L}\boldsymbol{I}_2, \boldsymbol{G} = \frac{V_d}{2L}\boldsymbol{K}$, and $\boldsymbol{P} = \frac{1}{2L}\boldsymbol{I}_2$, with $\boldsymbol{I}_2$ being the two-by-two identity matrix. The *abc* subscript has been dropped from $\boldsymbol{u}$ for convenience. Note that all other quantities, except for the input $\boldsymbol{u}$, are referred to the stationary orthogonal αβ-reference. The (reduced) Clarke transformation matrix

$$\boldsymbol{K} = \frac{2}{3} \begin{bmatrix} 1 & -\frac{1}{2} & -\frac{1}{2} \\ 0 & \frac{\sqrt{3}}{2} & -\frac{\sqrt{3}}{2} \end{bmatrix} \tag{4}$$

is used to transform the three-phase *abc* variables to αβ variables with $\boldsymbol{\xi}_{\alpha\beta} = \boldsymbol{K}\boldsymbol{\xi}_{abc}$.

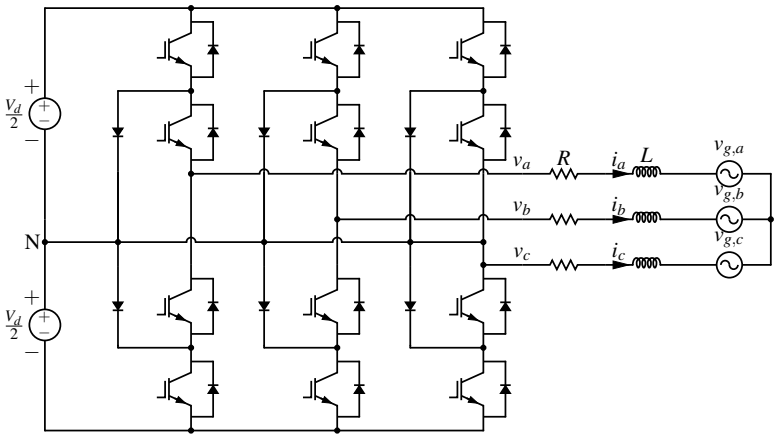

Fig. 1: Grid-connected three-phase three-level NPC converter.

Harmonic suppression strategy

The underlying idea of the proposed strategy is to include additional state variables that contain primarily the target frequencies. To do so, filters can be included in an augmented state-space representation of the plant. The outputs of the filters, which will be state variables, can then be penalised in the objective function. This will result in the magnitude of the target harmonics to be reduced.

Formulation of filter for additional states

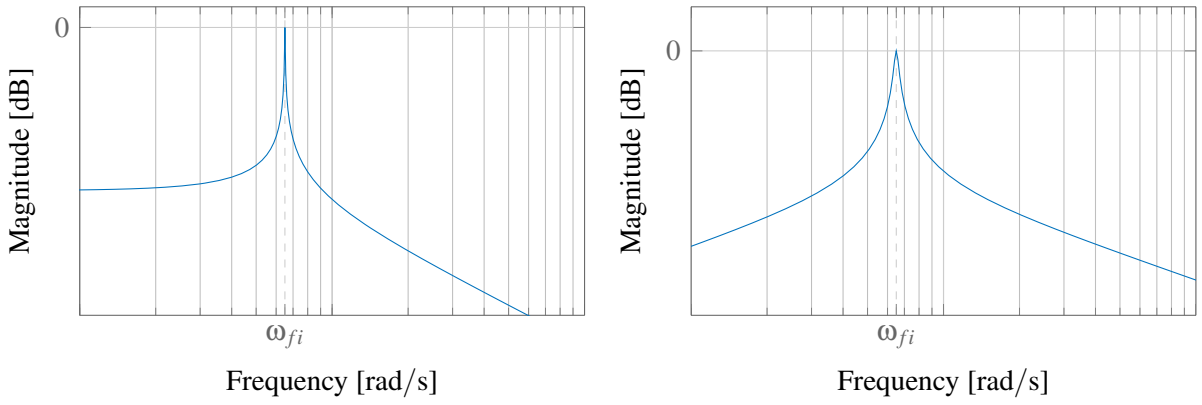

(a) Underdamped second-order low-pass filter.

(b) Band-pass filter.

Fig. 2: Frequency response of the second-order filters being considered.

One obvious choice of a suitable filter is to add resonant poles at certain target frequencies, $s = \pm j\omega_{fi}$, for $i = 1, 2, \ldots, n_f$, where n_f is the number of target frequencies. This results in the transfer function of the filter at ω_{fi} to have an infinite gain.

However, a pure resonant term is ill-suited for two reasons. Firstly, due to the spread spectrum of FCS-MPC, suppressing a harmonic at, say 250 Hz, can result in the harmonic content to be simply shifted to a close neighbouring frequency such as 253 Hz (preliminary simulations verified this claim). Secondly, when a pure resonant term is discretised and implemented digitally, it could move the resonant pole outside of the unit circle. To avoid these potential problems, some damping is added to the pole. The filter will then be a highly underdamped second-order low-pass filter, similar to an *LCL* filter. An alternative choice for the second-order low-pass filter would be a band-pass filter. The frequency response of the two filters (with unity gain) in consideration is shown in Fig. 2. The band-pass filter is chosen over the low-pass filter due to the fact that it attenuates all harmonics except the target harmonic, whereas the low-pass filter has a flat response up to the target frequency and only starts to significantly attenuate after the target frequency. The band-pass filter also allows for a more systematic design process, as the bandwidth can be used as a design parameter, whereas the damping required for the low-pass filter is difficult to choose.

The transfer function of a second-order band-pass filter is

$$H_{fi}(s) = \frac{H_{0i}\frac{\omega_{fi}}{Q_i}s}{s^2 + \frac{\omega_{fi}}{Q_i}s + \omega_{fi}^2}, \tag{5}$$

where ω_{fi}, Q_i and H_{0i} are the center frequency, quality factor, and gain, respectively, of the ith filter. The quality factor is used to adjust the bandwidth of the filter,

$$Q_i = \frac{\omega_{fi}}{\Delta\omega_{fi}}, \tag{6}$$

where $\Delta\omega_{fi}$ defines the bandwidth. The filter has a gain of $-3\,\mathrm{dB}$ at $\omega_{fi} \pm \frac{1}{2}\Delta\omega_{fi}$.

Note that two filters are required for each harmonic to be suppressed, one for each axis of the $\alpha\beta$-grid current. To include both filters in the dynamic model of the controller, the filters can be described by the continuous-time state-space representation

$$\frac{d\boldsymbol{x}_{fi}(t)}{dt} = \boldsymbol{F}_{fi}\boldsymbol{x}_{fi}(t) + \boldsymbol{G}_{fi}\boldsymbol{i}_{\alpha\beta}(t), \tag{7}$$

where the state variables include the filtered grid currents along with their derivatives,

$$\boldsymbol{x}_{fi}(t) = \begin{bmatrix} i_{\alpha,fi}(t) & \frac{di_{\alpha,fi}(t)}{dt} & i_{\beta,fi}(t) & \frac{di_{\beta,fi}(t)}{dt} \end{bmatrix}^{\mathrm{T}}. \tag{8}$$

The state and input matrices are defined as

$$\boldsymbol{F}_{fi} = \begin{bmatrix} 0 & 1 & 0 & 0 \\ -\omega_{fi}^2 & -\frac{\omega_{fi}}{Q_{fi}} & 0 & 0 \\ 0 & 0 & 0 & 1 \\ 0 & 0 & -\omega_{fi}^2 & -\frac{\omega_{fi}}{Q_{fi}} \end{bmatrix} \quad \text{and} \quad \boldsymbol{G}_{fi} = \begin{bmatrix} H_{0i}\frac{\omega_{fi}}{Q_{fi}} & 0 \\ -H_{0i}\left(\frac{\omega_{fi}}{Q_{fi}}\right)^2 & 0 \\ 0 & H_{0i}\frac{\omega_{fi}}{Q_{fi}} \\ 0 & -H_{0i}\left(\frac{\omega_{fi}}{Q_{fi}}\right)^2 \end{bmatrix}. \tag{9}$$

See [12] for details on state-space representations that include derivatives of the input.

Augmented state-space representation

The filter dynamics can easily be included in the dynamic model used by the controller. For suppressing n_f harmonics with the filters $\boldsymbol{F}_{fi}$, $\boldsymbol{G}_{fi}$, the state variables are the grid currents and the filters states,

$$\boldsymbol{x}_{aug}(t) = \begin{bmatrix} \boldsymbol{x}^{\mathrm{T}}(t) & \boldsymbol{x}_{f1}^{\mathrm{T}}(t) & \boldsymbol{x}_{f2}^{\mathrm{T}}(t) & \cdots & \boldsymbol{x}_{fn_f}^{\mathrm{T}}(t) \end{bmatrix}^{\mathrm{T}}, \tag{10}$$

which are described by the augmented state-space representation

$$\frac{d\boldsymbol{x}_{aug}(t)}{dt} = \boldsymbol{F}_{aug}\boldsymbol{x}_{aug}(t) + \boldsymbol{G}_{aug}\boldsymbol{u}(t) + \boldsymbol{P}_{aug}\boldsymbol{v}_g(t). \tag{11}$$

The augmented state-space matrices are defined as

$$\boldsymbol{F}_{aug} = \begin{bmatrix} \boldsymbol{F} & \mathbf{o}_{2\times4} & \mathbf{o}_{2\times4} & \cdots & \mathbf{o}_{2\times4} \\ \boldsymbol{G}_{f1} & \boldsymbol{F}_{f1} & \mathbf{o}_{4\times4} & \cdots & \mathbf{o}_{4\times4} \\ \boldsymbol{G}_{f2} & \mathbf{o}_{4\times4} & \boldsymbol{F}_{f2} & \cdots & \mathbf{o}_{4\times4} \\ \vdots & \vdots & & \ddots & \vdots \\ \boldsymbol{G}_{fn_f} & \mathbf{o}_{4\times4} & \mathbf{o}_{4\times4} & \cdots & \boldsymbol{F}_{fn_f} \end{bmatrix}, \quad \boldsymbol{G}_{aug} = \begin{bmatrix} \boldsymbol{G} \\ \mathbf{o}_{4\times3} \\ \mathbf{o}_{4\times3} \\ \vdots \\ \mathbf{o}_{4\times3} \end{bmatrix}, \quad \text{and} \quad \boldsymbol{P}_{aug} = \begin{bmatrix} \boldsymbol{P} \\ \mathbf{o}_{4\times2} \\ \mathbf{o}_{4\times2} \\ \vdots \\ \mathbf{o}_{4\times2} \end{bmatrix}. \tag{12}$$

The continuous-time state-space representation of (11) is discretised by using the exact discretisation:

$$\boldsymbol{A}_{aug} = e^{\boldsymbol{F}_{aug}T_s}, \quad \boldsymbol{B}_{aug} = -\boldsymbol{F}_{aug}{}^{-1}\left(\boldsymbol{I}_{2+4n_f} - \boldsymbol{A}_{aug}\right)\boldsymbol{G}_{aug}, \quad \text{and} \quad \boldsymbol{T}_{aug} = -\boldsymbol{F}_{aug}{}^{-1}\left(\boldsymbol{I}_{2+4n_f} - \boldsymbol{A}_{aug}\right)\boldsymbol{P}_{aug}, \tag{13}$$

with $e^{\boldsymbol{F}_{aug}T_s}$ being the matrix exponential of $\boldsymbol{F}_{aug}T_s$ and T_s being the sampling interval. The state variables can now be described with a discrete-time state-space representation of the plant:

$$\boldsymbol{x}_{aug}(k+1) = \boldsymbol{A}_{aug}\boldsymbol{x}_{aug}(k) + \boldsymbol{B}_{aug}\boldsymbol{u}(k) + \boldsymbol{T}_{aug}\boldsymbol{v}_g(k). \tag{14}$$

By using the augmented dynamic model, the controller is able to suppress harmonics by penalising the magnitude of the filter outputs.

Fundamental component compensation

Since the band-pass filters are non-ideal, the 50 Hz fundamental component will be present in the output spectra of the filters. The fundamental component of the grid current is also significantly larger than any other harmonic, and thus its presence in the filter outputs cannot be ignored. This has the effect that when the magnitudes of the filter outputs are penalised, with the intention of reducing the harmonic content at the target frequencies, the magnitude of the fundamental component will unintentionally be penalised too. This can be compensated for by setting the reference of the filter outputs equal to the filtered fundamental component:

$$i^*_{\alpha,fi}(t) = K_{fi}I^*_g \sin(\omega_1 t + \phi^*_g + \phi_{fi}) \quad \text{and} \quad i^*_{\beta,fi}(t) = -K_{fi}I^*_g \cos(\omega_1 t + \phi^*_g + \phi_{fi}), \tag{15}$$

where I^*_g and ϕ^*_g denote the amplitude and phase of the grid current reference. By doing so, the fundamental component in the filter output is ignored, resulting in only the target harmonic being penalised. The gain K_{fi} and phase ϕ_{fi} of the ith filter at the fundamental frequency can be calculated as $K_{fi} = \left|H_{fi}(j\omega_1)\right|$ and $\phi_{fi} = \angle H_{fi}(j\omega_1)$, where ω_1 is the fundamental angular frequency. Note that it is assumed that the fundamental component of the grid currents will be equal to their references during steady state.

Optimal Control

The finite-control-set model predictive control problem

By using the discrete-time model of (14), MPC predicts the evolution of the state variables $\boldsymbol{x}(l+1)$ over the finite horizon N_p as a function of the manipulated variables $\boldsymbol{u}(l)$, for $l = k, k+1, \ldots, k+N_p-1$. The switching sequence

$$\boldsymbol{U}(k) = \begin{bmatrix}\boldsymbol{u}^{\mathrm{T}}(k) & \boldsymbol{u}^{\mathrm{T}}(k+1) & \cdots & \boldsymbol{u}^{\mathrm{T}}(k+N_p-1)\end{bmatrix}^{\mathrm{T}} \tag{16}$$

is introduced as the switch positions of the converter over the prediction horizon, which is restricted to the set $\mathbb{U} = \mathcal{U} \times \mathcal{U} \times \ldots \times \mathcal{U} = \mathcal{U}^{N_p}$.

The user-defined control objectives are mapped into an objective function. In this paper, the control objectives are reference tracking and reduction of switching frequency, which can be stated as

$$J(\boldsymbol{x}_{aug}(k), \boldsymbol{U}(k)) = \sum_{l=k}^{k+N_p-1} \left\|\boldsymbol{x}^*_{aug}(l+1) - \boldsymbol{x}_{aug}(l+1)\right\|^2_{\boldsymbol{Q}} + \lambda_u \left\|\boldsymbol{u}(l) - \boldsymbol{u}(l-1)\right\|^2_2. \tag{17}$$

The term $\left\|\boldsymbol{x}^*_{aug}(l+1) - \boldsymbol{x}_{aug}(l+1)\right\|^2_{\boldsymbol{Q}}$ is a vector norm weighted with the diagonal penalty matrix $\boldsymbol{Q}$, which penalises the (tracking) error between the reference $\boldsymbol{x}^*_{aug}(l+1)$ and the predicted state $\boldsymbol{x}_{aug}(l+1)$. The second term $\left\|\boldsymbol{u}(l) - \boldsymbol{u}(l-1)\right\|^2_2$ represents the switching effort, which is penalised by the weighting factor $\lambda_u > 0$. The penalty matrix $\boldsymbol{Q}$ is used to prioritise the reference tracking of different state variables, and the weighting factor λ_u adjusts the trade-off between the tracking error and the switching frequency.

The entries on the diagonal of the penalty matrix $\boldsymbol{Q}$ that refer to the filter outputs can now be adjusted according to how aggressively the controller should suppress harmonics. Note that the time derivatives of the filter outputs, (see the second and forth states in (8)) are not penalised by setting their respective penalties to zero.

The minimization of (17) over the switching sequence $\boldsymbol{U}(k)$ yields an optimal solution that results in the optimal

behaviour of the system, i.e.,

$$\boldsymbol{U}_{opt}(k) = \arg\min_{\boldsymbol{U}(k)} \quad J(\boldsymbol{x}_{aug}(k), \boldsymbol{U}(k)) \tag{18a}$$

$$\text{subject to } \boldsymbol{U}(k) \in \mathbb{U}. \tag{18b}$$

Once the optimal solution has been calculated, only the switch position at the current time step (i.e., $\boldsymbol{u}(k)$ in (16)) is applied. The remaining switch positions are discarded and the entire optimisation problem is repeated at the following sampling instant. This is known as the *receding horizon* principle and introduces feedback, making the controller robust to noise and disturbances.

The integer least-squares reformulation

The optimisation problem of (18) is usually solved by enumerating *all* possible switching sequences in $\mathbb{U}$. However, since the number of possible switching sequences grows exponentially as the length of the horizon increases ($|\mathbb{U}| = 3^{3N_p}$), enumeration is only feasible for prediction horizons of lengths 1 or 2.

To reformulate the underlying optimisation problem, the objective function is rewritten in the quadratic form [2]:

$$J = \boldsymbol{U}^{\mathrm{T}}(k)\boldsymbol{H}\boldsymbol{U}(k) + 2\boldsymbol{\Theta}^{\mathrm{T}}(k)\boldsymbol{U}(k) + \theta(k), \tag{19}$$

where

$$\boldsymbol{H} = \boldsymbol{\Upsilon}^{\mathrm{T}}\tilde{\boldsymbol{Q}}\boldsymbol{\Upsilon} + \lambda_u \boldsymbol{S}^{\mathrm{T}}\boldsymbol{S} \tag{20}$$

$$\boldsymbol{\Theta}(k) = \boldsymbol{\Upsilon}^{\mathrm{T}}\tilde{\boldsymbol{Q}}\left(\boldsymbol{\Gamma}\boldsymbol{x}(k) + \boldsymbol{\Psi}\boldsymbol{V}_g(k) - \boldsymbol{X}^*_{aug}(k)\right) - \lambda_u \boldsymbol{S}^{\mathrm{T}}\boldsymbol{E}\boldsymbol{u}(k-1) \tag{21}$$

$$\theta(k) = \left\|\boldsymbol{\Gamma}\boldsymbol{x}(k) + \boldsymbol{\Psi}\boldsymbol{V}_g(k) - \boldsymbol{X}^*_{aug}(k)\right\|^2_{\tilde{\boldsymbol{Q}}} + \lambda_u \left\|\boldsymbol{E}\boldsymbol{u}(k-1)\right\|_2^2, \tag{22}$$

where $\boldsymbol{X}^*(k)$ and $\boldsymbol{V}_g(k)$ are introduced as the state reference and the grid voltage over the prediction horizon, respectively:

$$\boldsymbol{X}^*_{aug}(k) = \begin{bmatrix}\boldsymbol{x}^{*\mathrm{T}}_{aug}(k+1) & \boldsymbol{x}^{*\mathrm{T}}_{aug}(k+2) & \cdots & \boldsymbol{x}^{*\mathrm{T}}_{aug}(k+N_p)\end{bmatrix}^{\mathrm{T}} \tag{23}$$

$$\boldsymbol{V}_g(k) = \begin{bmatrix}\boldsymbol{v}^{\mathrm{T}}_g(k) & \boldsymbol{v}^{\mathrm{T}}_g(k+1) & \cdots & \boldsymbol{v}^{\mathrm{T}}_g(k+N_p-1)\end{bmatrix}^{\mathrm{T}}. \tag{24}$$

The penalty matrix over the prediction horizon is defined as $\tilde{\boldsymbol{Q}} = \mathrm{diag}\,(\boldsymbol{Q}, \boldsymbol{Q}, \ldots, \boldsymbol{Q})$. Matrices $\boldsymbol{\Upsilon}$, $\boldsymbol{\Gamma}$, $\boldsymbol{\Psi}$, $\boldsymbol{S}$, and $\boldsymbol{E}$ are defined in the appendix.

After completing the squares in (19) and neglecting terms that are constant during minimisation, the optimisation problem in (18) can be stated as an integer least-squares (ILS) problem [2]:

$$\boldsymbol{U}_{opt}(k) = \arg\min_{\boldsymbol{U}(k)} \quad \|\boldsymbol{V}\boldsymbol{U}_{unc}(k) - \boldsymbol{V}\boldsymbol{U}(k)\|_2^2 \tag{25a}$$

$$\text{subject to } \boldsymbol{U}(k) \in \mathbb{U}, \tag{25b}$$

where

$$\boldsymbol{U}_{unc}(k) = -\boldsymbol{H}^{-1}\boldsymbol{\Theta}(k) \tag{26}$$

is known as the unconstrained optimum (i.e., the optimal solution if the integer constraints of (25b) are relaxed). The lower-triangular matrix $\boldsymbol{V}$ is known as the *lattice generator* matrix and is obtained from the Cholesky decomposition of $\boldsymbol{H}^{-1}$, $\boldsymbol{V}^{-1}\boldsymbol{V}^{-\mathrm{T}} = \boldsymbol{H}^{-1}$.

The ILS problem of (25) can be solved with a branch-and-bound method known as sphere decoding. By only requiring to evaluate a small subset of possible solutions in $\mathbb{U}$, sphere decoding finds the optimal solution $\boldsymbol{U}_{opt}(k)$ orders of magnitude quicker than the usual enumeration approach [5]. This enables horizons beyond $N_p > 10$ to be practically feasible. As the focus of this paper is not on sphere decoding, and for the sake of brevity, details of sphere decoding are omitted; for details on the theory of sphere decoding, see [13]. Sphere decoding algorithms tailored to FCS-MPC can be found in [2] (a recursive algorithm) and in [7] (a non-recursive

algorithm used in a practical system).

Control algorithm

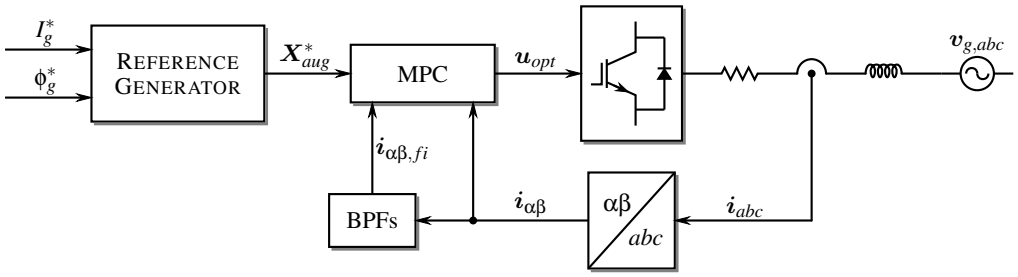

Fig. 3: Block diagram of the system. The band-pass filters are denoted by BPFs.

A block diagram of the system is shown in Fig. 3. The control algorithm is summarised below.

1. Calculate the grid currents and filter output references over the horizon, i.e $\boldsymbol{X}_{aug}^*$, given the desired fundamental component's amplitude I_g^* and phase ϕ_g^*.
2. Measure the *abc* grid currents and transform them to the stationary αβ-reference frame, which is then passed to the band-pass filters (BPFs).
3. Formulate the ILS problem of (25).
4. Solve the ILS problem using sphere decoding and apply the optimal switch position $\boldsymbol{u}_{opt}(k)$ to the converter.

Simulation Results

The efficacy of the harmonic suppression method will be demonstrated with simulations. The controller and plant parameters are summarized in Table I.

Table I: PLANT PARAMETERS

Variable	Description	Value
T_s	Controller sampling interval	50 µs
R	Load resistance	16.5 mΩ
L	Load inductance	933.49 µH
V_d	dc-link voltage	4.84 kV
$V_{g,LL}$	Grid line-to-line voltage	3.15 kV (rms)
S_{rated}	Rated power	9 MVA
I_{rated}	Rated line current	1.647 kA (rms)

Unless otherwise stated, the gains of all band-pass filters are set to 10 and their bandwidth to 75 Hz. The operating conditions are set to rated values and unity power factor, meaning $I_g^* = \sqrt{2} I_{rated}$ and $\phi_g^* = 0^\circ$ in Fig. 3. The weighting factor is tuned so that an average device switching frequency of $f_{sw} = 300$ Hz is obtained.

Suppression of a single harmonic

As a point of reference, the unsuppressed current spectra, grid currents, and switch positions of $N_p = 1$ are shown in Fig. 4. Note the noisy current spectrum of FCS-MPC. Due to this, the power of the harmonics are lumped together into the nearest integer multiple of the fundamental frequency when the magnitude of a harmonic is computed. For example, when computing the magnitude of the 11th harmonic (at 550 Hz), the energy of the harmonics from 525 Hz to 575 Hz are also included, i.e., $\hat{i}_{11} = \sqrt{\sum_{n\in\mathcal{N}} \hat{i}_n^2}$, where $\hat{i}_n$ is the magnitude of the nth harmonic and $\mathcal{N}$ is the index set that refers to the harmonics from 525 Hz to 575 Hz. Note that n is not restricted to an integer.

The harmonic at 550 Hz is chosen to be suppressed. In Table II, the simulation results of prediction horizons $N_p = 1$ and 8 are presented. Simulations are done without and with harmonic suppression, where the weight on the filter output is denoted by w_1. It can be observed in both cases that longer horizons decrease the total harmonic distortion (THD) of the current and achieve slightly better attenuation of the harmonic at 550 Hz. For $N_p = 1$, the harmonic was attenuated by 65 %, whereas for $N_p = 8$ the harmonic was attenuated by 70 % and the THD of the current was decreased by 20 % relative to $N_p = 1$. A dip in the noise floor can be observed in the spectra of Fig. 5a and Fig. 6a where the harmonic is suppressed. It is also observed that the current THD increases when harmonics are suppressed. Without harmonic suppression, for a given λ_u, the harmonic spectrum of the current is optimal in the sense that the tracking error (which relates to THD) is minimized. When adding the additional terms that suppress harmonics in the objective function, the focus on reference tracking decreases and therefore the THD of the current increases.

It is also interesting to note that the noise floor of $N_p = 8$ is lower than that of $N_p = 1$. This can be attributed to the longer horizon being more periodical, which focuses more harmonic power into integer multiples of the fundamental harmonic, see also [5].

Table II: SIMULATION RESULTS.

	NO SUPPRESSION				SUPPRESSION AT 550 Hz				
N_p	f_{sw}	I_{THD}	$\hat{i}_{11}$	λ_u	f_{sw}	I_{THD}	$\hat{i}_{11}$	λ_u	w_1
1	299 Hz	4.59 %	24.25 A	1.78×10^4	299 Hz	5.55 %	8.46 A	2.2×10^4	2.5
8	300 Hz	3.97 %	22.41 A	9.8×10^4	301 Hz	4.42 %	6.73 A	14.8×10^4	0.43

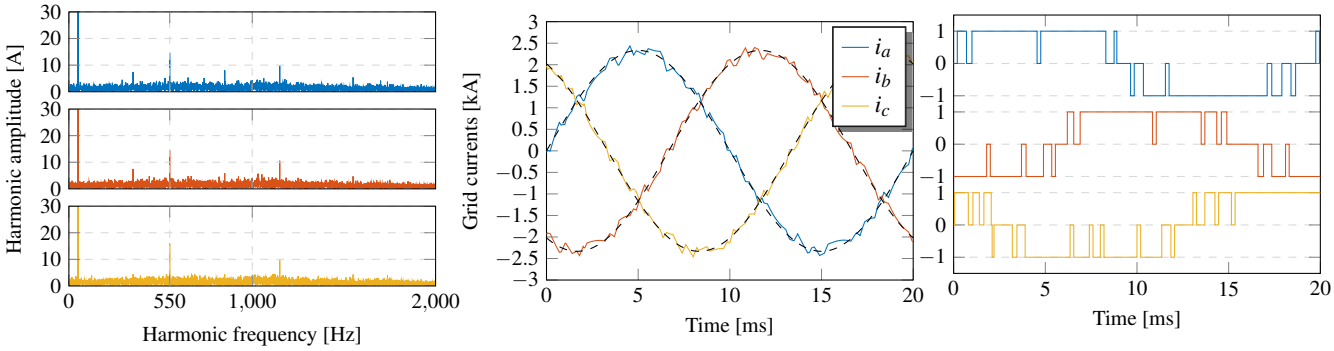

(a) Grid current spectra. (b) Grid current waveforms. (c) Switch positions.

Fig. 4: Single-step horizon without harmonic suppression.

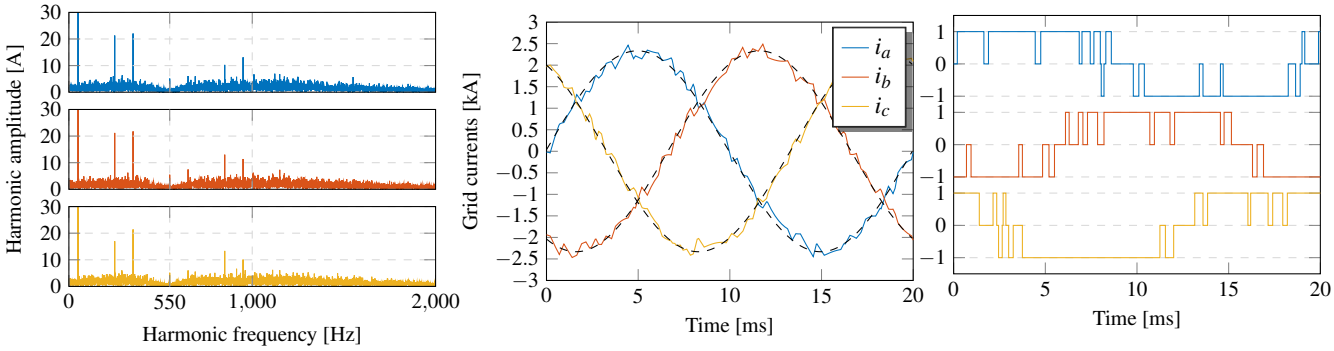

(a) Grid current spectra. (b) Grid currents waveforms. (c) Switch positions.

Fig. 5: Single-step horizon with harmonic suppression at 550 Hz.

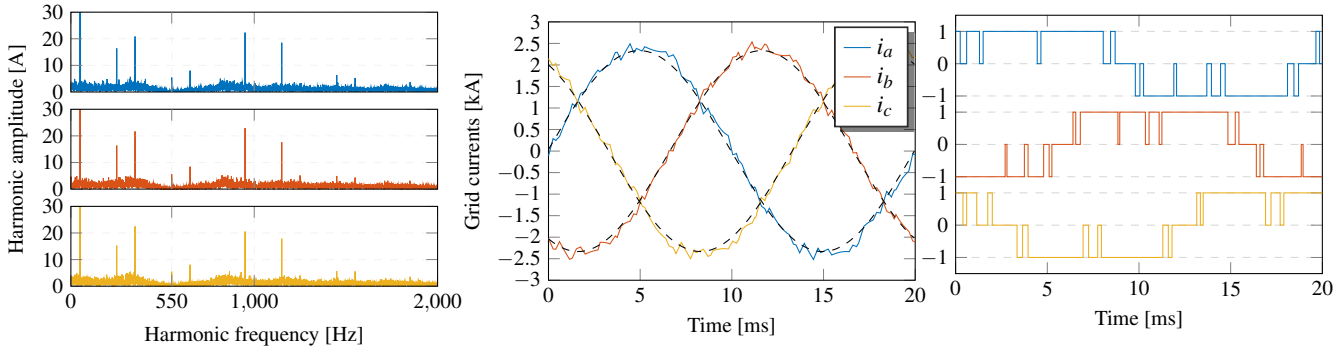

(a) Grid current spectra.

(b) Grid current waveforms.

(c) Switch positions.

Fig. 6: 8-step horizon with harmonic suppression at 550 Hz.

Suppression of multiple harmonics

Multiple harmonics can also be suppressed, as illustrated in Fig. 8 where the grid currents spectra are shown for $N_p = 8$. The harmonics at 250 Hz and 550 Hz were suppressed, with the weights being $w_1 = w_2 = 1$. The harmonic at 250 Hz was reduced from 17.8 A to 5.47 A, and the harmonic at 550 Hz was reduced from 22.41 A to 6.84 A. A switching frequency of 299 Hz was achieved at a weighting factor of $\lambda_u = 31.2 \times 10^4$. The THD of the current was 4.47 % (increasing from the 3.97 % achieved without harmonic suppression). The dip in the noise floor can again be observed in Fig. 8.

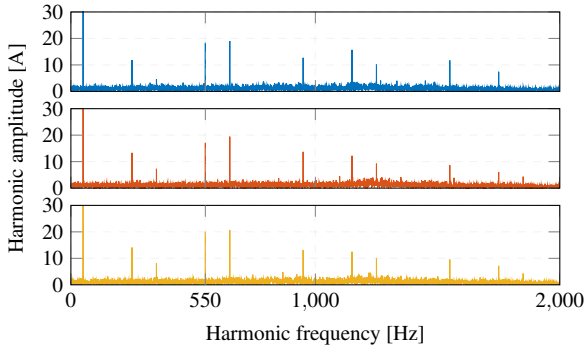

Fig. 7: Grid current spectra without harmonic suppression for $N_p = 8$.

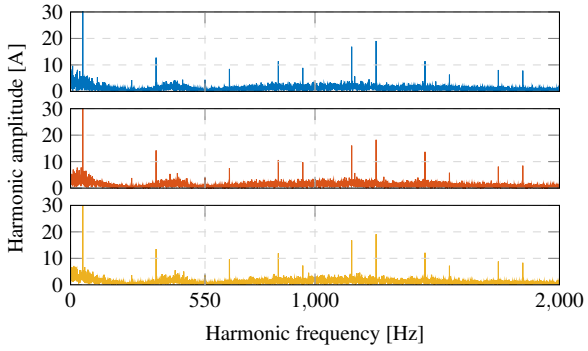

Fig. 8: Grid current spectra for multiple harmonic suppressions for $N_p = 8$.

Conclusions

This paper proposed a method for long-horizon FCS-MPC to suppress specific harmonics. The proposed method can easily be included in the control problem by simply augmenting the dynamic model of the controller with band-pass filters, while no further modifications to the controller are required.

Simulations of a grid-connected converter verified that the method does successfully suppress target harmonics. For horizons 1 and 8, the target harmonics were suppressed by 65 % and 70 %, respectively. The performance benefit of long horizons is still present with the suppression method, as it was seen that $N_p = 8$ decreased the THD of the current by 20 % relative to $N_p = 1$.

Appendix

$$\boldsymbol{\Gamma} = \begin{bmatrix} \boldsymbol{A}_{aug} \\ \boldsymbol{A}_{aug}^2 \\ \vdots \\ \boldsymbol{A}_{aug}^{N_p} \end{bmatrix}, \boldsymbol{\Upsilon} = \begin{bmatrix} \boldsymbol{B}_{aug} & \mathbf{o}_{(2+4n_f)\times 3} & \cdots & \mathbf{o}_{(2+4n_f)\times 3} \\ \boldsymbol{A}_{aug}\boldsymbol{B}_{aug} & \boldsymbol{B}_{aug} & \cdots & \mathbf{o}_{(2+4n_f)\times 3} \\ \vdots & \vdots & \ddots & \vdots \\ \boldsymbol{A}_{aug}^{N_p-1}\boldsymbol{B}_{aug} & \boldsymbol{A}_{aug}^{N_p-2}\boldsymbol{B}_{aug} & \cdots & \boldsymbol{B}_{aug} \end{bmatrix}, \boldsymbol{\Psi} = \begin{bmatrix} \boldsymbol{T}_{aug} & \mathbf{o}_{(2+4n_f)\times 2} & \cdots & \mathbf{o}_{(2+4n_f)\times 2} \\ \boldsymbol{A}_{aug}\boldsymbol{T}_{aug} & \boldsymbol{T}_{aug} & \cdots & \mathbf{o}_{(2+4n_f)\times 2} \\ \vdots & \vdots & \ddots & \vdots \\ \boldsymbol{A}_{aug}^{N_p-1}\boldsymbol{T}_{aug} & \boldsymbol{A}_{aug}^{N_p-2}\boldsymbol{T}_{aug} & \cdots & \boldsymbol{T}_{aug} \end{bmatrix},$$

$$\boldsymbol{S} = \begin{bmatrix} \boldsymbol{I}_3 & \mathbf{o}_{3\times 3} & \cdots & \mathbf{o}_{3\times 3} \\ -\boldsymbol{I}_3 & \boldsymbol{I}_3 & \cdots & \mathbf{o}_{3\times 3} \\ \mathbf{o}_{3\times 3} & -\boldsymbol{I}_3 & \cdots & \mathbf{o}_{3\times 3} \\ \vdots & \vdots & \ddots & \vdots \\ \mathbf{o}_{3\times 3} & \mathbf{o}_{3\times 3} & \cdots & \boldsymbol{I}_3 \end{bmatrix} \text{ and } \boldsymbol{E} = \begin{bmatrix} \boldsymbol{I}_3 \\ \mathbf{o}_{3\times 3} \\ \mathbf{o}_{3\times 3} \\ \vdots \\ \mathbf{o}_{3\times 3} \end{bmatrix}.$$

References

[1] P. Cortes, M. Kazmierkowski, R. Kennel, D. Quevedo, and J. Rodriguez, "Predictive Control in Power Electronics and Drives," *IEEE Transactions on Industrial Electronics*, vol. 55, no. 12, pp. 4312–4324, Dec. 2008.

[2] T. Geyer and D. E. Quevedo, "Multistep Finite Control Set Model Predictive Control for Power Electronics," *IEEE Transactions on Power Electronics*, vol. 29, no. 12, pp. 6836–6846, Dec. 2014.

[3] T. Geyer, *Model Predictive Control of High Power Convertersand Industrial Drives*. Chichester, UK: John Wiley & Sons, Nov. 2016.

[4] D. E. Quevedo, R. P. Aguilera, and T. Geyer, "Predictive Control in Power Electronics and Drives: Basic Concepts, Theory, and Methods," in *Advanced and Intelligent Control in Power Electronics and Drives*, T. Orłowska-Kowalska, F. Blaabjerg, and J. Rodríguez, Eds. Springer International Publishing, 2014, vol. 531, pp. 181–226.

[5] T. Geyer and D. E. Quevedo, "Performance of Multistep Finite Control Set Model Predictive Control for Power Electronics," *IEEE Transactions on Power Electronics*, vol. 30, no. 3, pp. 1633–1644, Mar. 2015.

[6] A. Ayad, P. Karamanakos, and R. Kennel, "Direct Model Predictive Current Control Strategy of Quasi-Z-Source Inverters," *IEEE Transactions on Power Electronics*, vol. 32, no. 7, pp. 5786–5801, Jul. 2017.

[7] M. Dorfling, H. Mouton, P. Karamanakos, and T. Geyer, "Experimental evaluation of sphere decoding for long-horizon direct model predictive control," in *European Conference on Power Electronics and Applications (EPE'17 ECCE Europe)*. IEEE, Sep. 2017.

[8] D. N. Walker, *Torsional Vibration of Turbomachinery*, ser. McGraw-Hill engineering reference. New York, NY: McGraw-Hill, 2004.

[9] P. Cortes, J. Rodriguez, D. E. Quevedo, and C. Silva, "Predictive Current Control Strategy With Imposed Load Current Spectrum," *IEEE Transactions on Power Electronics*, vol. 23, no. 2, pp. 612–618, Mar. 2008.

[10] R. P. Aguilera, P. Acuna, P. Lezana, G. Konstantinou, B. Wu, S. Bernet, and V. G. Agelidis, "Selective Harmonic Elimination Model Predictive Control for Multilevel Power Converters," *IEEE Transactions on Power Electronics*, vol. 32, no. 3, pp. 2416–2426, Mar. 2017.

[11] J.-H. Hours, M. N. Zeilinger, R. Gondhalekar, and C. N. Jones, "Constrained Spectrum Control," *IEEE Transactions on Automatic Control*, vol. 60, no. 7, pp. 1969–1974, Jul. 2015.

[12] K. Ogata, *Modern Control Engineering*, 5th ed. Boston, Mass.: Pearson, 2010.

[13] B. Hassibi and H. Vikalo, "On the Sphere-decoding Algorithm I. Expected Complexity," *IEEE Transactions on Signal Processing*, vol. 53, no. 8, pp. 2806–2818, Aug. 2005.